

# Controlling Excitation Localization in Waveguide QED Systems

C.-Y. Lee<sup>1,\*</sup>, K.-T. Lin<sup>2,†</sup>, G.-D. Lin<sup>1,2,3</sup>, and H. H. Jen<sup>4,1</sup>

<sup>1</sup>*Physics Division, National Center for Theoretical Sciences, Taipei 10617, Taiwan*

<sup>2</sup>*Trapped-Ion Quantum Computing Laboratory, Hon Hai Research Institute, Taipei 11492, Taiwan*

<sup>3</sup>*Department of Physics and Center for Quantum Science and Engineering, National Taiwan University, Taipei 10617, Taiwan*

<sup>4</sup>*Institute of Atomic and Molecular Sciences, Academia Sinica, Taipei 10617, Taiwan*

We theoretically investigate excitation dynamics in one-dimensional arrays of quantum emitters coupled to a waveguide, focusing on localization and long-time population trapping. By combining time-domain simulations with spectral analysis of an effective non-Hermitian Hamiltonian, we identify two distinct mechanisms that give rise to localization: geometry-induced subradiance and disorder-induced Anderson-like confinement. Spatially modulated emitter arrangements—such as single- and double-Gaussian transverse profiles—enable long-lived subradiant modes even in the absence of disorder, with decay rates that can be finely controlled via geometric parameters. In contrast, localization in uniform arrays emerges only when disorder breaks spatial symmetry and suppresses collective emission through interference. We track the crossover between geometric and disorder-induced regimes, finding that double-Gaussian profiles exhibit clear spatial signatures of this transition, while single-Gaussian configurations display more gradual changes. These results establish geometry and disorder as complementary tools for engineering long-lived quantum states in waveguide QED systems, with direct relevance for scalable implementations in photonic platforms.

## I. INTRODUCTION

Waveguide quantum electrodynamics (QED) provides a versatile platform for exploring light-matter interactions in low-dimensional, open quantum systems [1–15]. Arrays of quantum emitters coupled to one-dimensional (1D) photonic reservoirs exhibit rich collective phenomena, including super-radiance, subradiance, and photon-mediated long-range interactions [6, 10, 16–19].

A central challenge in such systems is understanding and controlling excitation localization, i.e., the long-time retention of population within the emitter array. In conventional models, localization typically arises from disorder-induced interference, as in Anderson localization [20]. However, in open systems with non-Hermitian dynamics, engineered geometry can also induce localization via spatially inhomogeneous coupling, leading to the formation of subradiant modes [21–35] that are protected from collective decay. Despite extensive studies on disorder-induced localization in photonic and atomic systems [36–42], the role of emitter geometry in waveguide QED remains underexplored. Existing works often fix emitter positions, treating geometry as a static design choice, rather than as a tunable parameter for engineering localization.

In this work, we investigate population trapping in 1D arrays of quantum emitters coupled to a waveguide, by performing a systematic comparison of three spatial configurations: linear, single-Gaussian, and double-Gaussian transverse profiles. Disorder is introduced along the propagation axis, and localization behavior is analyzed through time-domain simulations and spectral decomposition of an effective non-Hermitian Hamiltonian [43]. The imaginary parts of the eigenvalues determine the decay rates of collective modes, enabling the identification of dominant long-lived eigenstates responsible for excitation retention.

Our results show that localization originates from two qual-

itatively distinct mechanisms: geometry-induced subradiance and disorder-induced localization, with a crossover behavior observed as disorder strength increases. The transition is subtle in single-Gaussian structures, but becomes more pronounced in double-Gaussian configurations that exhibit clear spatial signatures of the crossover. We further examine how localization depends on system size and find that structured emitter geometries—such as single- and double-Gaussian profiles—exhibit greater robustness and sustained population trapping than uniform linear arrays, especially in the weak-disorder regime.

These findings provide new insights into controllable radiative dynamics in waveguide QED and offer practical design principles for suppressing decoherence in quantum optical networks. The predicted behaviors are accessible using current experimental platforms, including superconducting qubits [44, 45], cold atoms coupled to nanophotonic waveguides [46, 47], and quantum dots in photonic crystals [3].

## II. THEORETICAL MODEL

We consider a 1D array of  $N$  identical two-level quantum emitters, with ground state  $|g\rangle$  and excited state  $|e\rangle$ , separated by a transition frequency  $\omega_{eg}$ , and coupled to a photonic waveguide, as illustrated in Fig. 1. In this setup, the transverse positions  $y_\mu$  of the emitters can be varied to produce inhomogeneous waveguide-emitter couplings, allowing control over the collective relaxation dynamics of the system. The system's dynamics in the interaction picture are governed by the Lindblad master equation [48, 49]:

$$\begin{aligned} \frac{d\rho}{dt} = & -i[H, \rho] - \frac{\gamma_0}{4} \sum_{\mu, \nu=1}^N e^{-(y_\mu + y_\nu)/\xi_c} e^{-ik_{eg}|x_\mu - x_\nu|} \\ & \times (\sigma_\mu^\dagger \sigma_\nu \rho + \rho \sigma_\mu^\dagger \sigma_\nu - 2\sigma_\nu \rho \sigma_\mu^\dagger) \end{aligned} \quad (1)$$

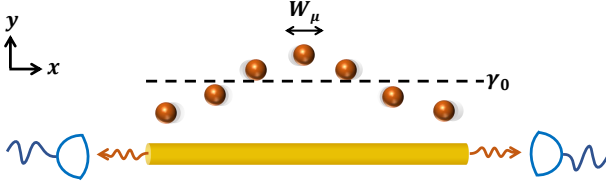


FIG. 1. Schematic of the system under consideration: a one-dimensional array of quantum emitters symmetrically coupled to a waveguide. Different transverse emitter geometries are realized by introducing position-dependent displacements  $y_\mu$ . The coupling rate  $\gamma_0$  is defined with respect to a reference position relative to the waveguide, as illustrated.

with the coherent interactions described by

$$H = -i\frac{\gamma_0}{4} \sum_{\mu \neq \nu} \sum_{v=1}^N e^{-(y_\mu + y_\nu)/\xi_c} \left( e^{ik_{eg}|x_\mu - x_\nu|} \sigma_\mu^\dagger \sigma_\nu - \text{H.c.} \right), \quad (2)$$

where  $\sigma_\mu^\dagger \equiv |e\rangle_\mu \langle g|$  is the dipole raising operator, and  $\gamma_0$  denotes the emitter-waveguide coupling strength. This master equation is derived under the Born-Markov approximation [50], and applies to 1D photonic reservoirs that mediate long-range dipole-dipole interactions [51]. The parameters  $\xi_c$  and  $k_{eg}$  represent the characteristic decay length and photon wavevector, respectively, where  $k_{eg} \equiv \omega_{eg}/v$  and  $v$  is the group velocity of the guided mode. For simplicity, we set  $\xi_c = 1$  throughout this work, so that all lengths and coupling expressions are normalized by the evanescent decay length. The spatially inhomogeneous coupling arises from the evanescent nature of the guided mode, which decays exponentially with transverse displacement from the waveguide.

To characterize the interaction range, we define the dimensionless parameter  $\xi \equiv k_{eg}|x_{\mu+1} - x_\mu|$ , which corresponds to the normalized inter-emitter spacing along the propagation direction. The emitters are positioned uniformly along the propagation axis, such that the inter-emitter spacing is fixed ( $\xi = \text{const}$ ). However, their transverse positions  $y_\mu$  are allowed to vary, leading to position-dependent coupling strengths with the photonic waveguide. This geometry preserves the one-dimensional topology of the system, while enabling spatially inhomogeneous interactions through transverse displacement.

We restrict our analysis to the single-excitation subspace, which fully describes the system dynamics under initial single-excitation conditions. The general state can be written as:  $|\Psi(t)\rangle = \sum_{\mu=1}^N a_\mu(t) |\psi\rangle_\mu$ , where  $|\psi\rangle_\mu = |e\rangle_\mu |g\rangle^{\otimes(N-1)}$  denotes a single excitation localized on the  $\mu$ -th emitter. Within this subspace, the effective non-Hermitian Hamiltonian takes the form [6, 52]:

$$H_{\text{eff}} = -i\frac{\gamma_0}{4} \sum_{\mu \neq \nu} \sum_{v=1}^N e^{-(y_\mu + y_\nu)} e^{ik_{eg}|x_\mu - x_\nu|} \sigma_\mu^\dagger \sigma_\nu - i\frac{\gamma_0}{2} \sum_{v=1}^N e^{-2y_v} \sigma_v^\dagger \sigma_v. \quad (3)$$

To study the effect of imperfections, we introduce static disorder  $W_\mu \in \pi[-\bar{\omega}, \bar{\omega}]$ , modeling onsite phase fluctuations along the waveguide axis. This leads to a Schrödinger-type equation governing the time evolution of the excitation amplitudes:

$$\begin{aligned} \dot{a}_\mu(t) = & -\frac{\gamma_0}{2} \sum_{\mu < \nu} e^{-(y_\mu + y_\nu)} e^{i|\mu - \nu|\xi - i(W_\mu - W_\nu)} a_\nu(t) \\ & -\frac{\gamma_0}{2} \sum_{\mu > \nu} e^{-(y_\mu + y_\nu)} e^{i|\mu - \nu|\xi - i(W_\nu - W_\mu)} a_\nu(t) \\ & -\frac{\gamma_0}{2} e^{-2y_\mu} a_\mu(t). \end{aligned} \quad (4)$$

In the following sections, we analyze the time evolution of  $a_\mu(t)$  under various array configurations and examine how disorder influences localization and excitation transport in geometrically structured one-dimensional emitter arrays.

### III. GEOMETRY-INDUCED LOCALIZATION AND MODE ANALYSIS

In this section, we investigate how the geometry of emitter arrays influences localization phenomena and long-time excitation trapping. We consider a system of  $N = 101$  emitters with uniform inter-emitter spacing  $\xi$ , and prepare the initial state as a symmetric Dicke state, in which the excitation is uniformly distributed across the array.

#### A. Localization Induced by Varying Inter-Emitter Spacing

We first examine how localization depends on the inter-emitter spacing  $\xi$ , keeping the transverse displacement parameters fixed at  $\eta = 0.05$  and  $\sigma = 0.2$  for the single-Gaussian profile, and  $\sigma = 0.075$  for the double-Gaussian case.

For the single-Gaussian configuration, defined as

$$y_\mu = 2\eta \exp\left(-\frac{(\mu/N - 1/2)^2}{2\sigma^2}\right) - \eta, \quad (5)$$

the remaining population  $P(t) = \sum_\mu |a_\mu(t)|^2$  exhibits monotonic decay for  $\xi = 0.1\pi$ , as shown in Fig. 2(a). At  $\xi = 0.15\pi$ , the decay slows considerably, and a finite fraction of the excitation persists at long times. When  $\xi$  is increased to  $0.2\pi$ , an even larger fraction survives; however, the spatial distribution  $P_n(t) = |a_n(t)|^2$  at  $\gamma_0 t = 10^4$  deviates significantly from the original Gaussian profile [Fig. 2(b)].

A similar trend is observed in the double-Gaussian configuration, described by

$$\begin{aligned} y_\mu = & 2\eta \exp\left(-\frac{(\mu/N - 1/4)^2}{2\sigma^2}\right) \\ & + 2\eta \exp\left(-\frac{(\mu/N - 3/4)^2}{2\sigma^2}\right) - \eta. \end{aligned} \quad (6)$$

At  $\xi = 0.25\pi$ , the decay becomes markedly slower, and a non-negligible portion of the excitation remains at long times [Fig. 2(c)]. For larger values of  $\xi$ , the spatial profile becomes increasingly distorted [Fig. 2(d)].

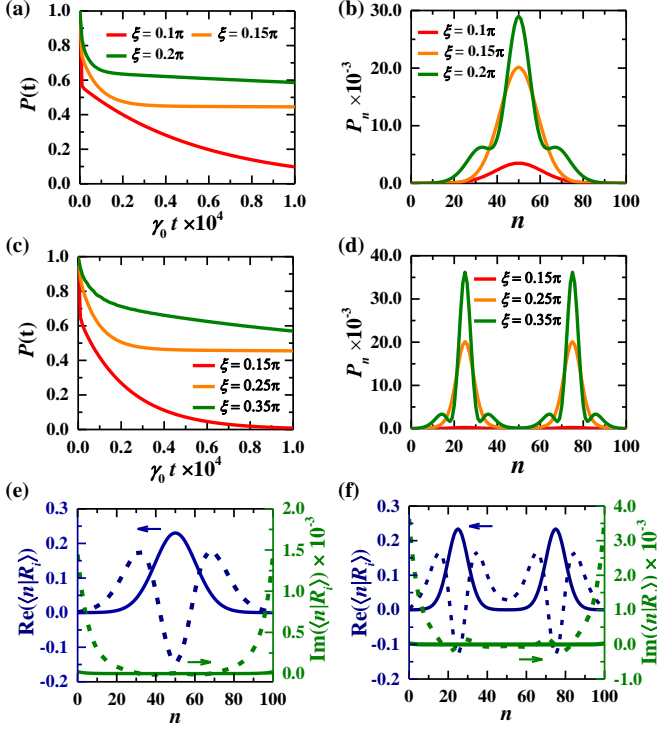


FIG. 2. (a) Time evolution of the remaining population in a single-Gaussian configuration for  $\xi = 0.1\pi, 0.15\pi$ , and  $0.2\pi$ . (b) Population distribution at time  $\gamma_0 t = 10^4$  corresponding to (a). (c) Temporal behavior of the remaining population in a double-Gaussian configuration for  $\xi = 0.15\pi, 0.25\pi$ , and  $0.35\pi$ . (d) Population distribution at  $\gamma_0 t = 10^4$  for cases in (c). (e) Eigenmodes contributing to the dynamics at  $\gamma_0 t = 10^4$  for the single-Gaussian case with  $\xi = 0.2\pi$ ; exactly two long-lived modes are involved. Solid and dashed lines represent the first mode and the second mode, respectively, with real and imaginary parts shown on the left and right axes. (f) Same as (e), but for the double-Gaussian configuration with  $\xi = 0.35\pi$ .

To uncover the mechanism behind the deviations in localization patterns at long times, we analyze the eigenmodes of the effective non-Hermitian Hamiltonian  $H_{\text{eff}}$  [Eq. (3)]. We compute its complex eigenvalues  $\lambda_i$  and corresponding biorthogonal eigenvectors  $\langle L_i |$  and  $| R_i \rangle$ , and project the initial state onto the eigenbasis as  $c_i = \langle L_i | \psi(0) \rangle$ . The time-dependent contribution of each mode is given by  $w_i(t) = |c_i e^{\lambda_i t}|^2$ , allowing us to identify how many modes remain populated at late times.

In the single-Gaussian case, for  $\xi = 0.1\pi$  and  $0.15\pi$ , only one long-lived mode contributes significantly, with decay rates  $\text{Im}(\lambda) = -8.8 \times 10^{-5}\gamma_0$  and  $-4.9 \times 10^{-7}\gamma_0$ , respectively. The corresponding population contributions at  $\gamma_0 t = 10^4$  are  $w(t) = 0.10$  and  $0.45$ . At  $\xi = 0.2\pi$ , the dynamics involve exactly two modes, with  $\text{Im}(\lambda_1) = -3.3 \times 10^{-9}\gamma_0$  and  $\text{Im}(\lambda_2) = -1.3 \times 10^{-5}\gamma_0$ , leading to deformation of the exci-

tation profile [Fig. 2(e)]. The contribution of the first mode is  $w_1(t) = 0.38$ , and the second mode contributes  $w_2(t) = 0.20$ .

In the double-Gaussian case, the system is again dominated by a single eigenmode at  $\xi = 0.15\pi$  and  $\xi = 0.25\pi$ , with decay rates  $\text{Im}(\lambda) = -2.2 \times 10^{-4}\gamma_0$  and  $-6.9 \times 10^{-7}\gamma_0$ , respectively. The population contribution at  $\gamma_0 t = 10^4$  is  $w(t) = 0.0079$  at  $\xi = 0.15\pi$  and  $w(t) = 0.46$  at  $\xi = 0.25\pi$ . At  $\xi = 0.35\pi$ , two long-lived modes contribute, with  $\text{Im}(\lambda_1) = -3.2 \times 10^{-9}\gamma_0$  and  $\text{Im}(\lambda_2) = -3.1 \times 10^{-5}\gamma_0$ , resulting in a visibly deformed spatial profile [Fig. 2(f)]. The contribution of the first mode is  $w_1(t) = 0.38$ , and the second mode is  $w_2(t) = 0.19$ .

These results show that the geometry of the emitter array significantly affects long-time localization by shaping the system's spectral structure. Specifically, subradiant eigenmodes with exceptionally small decay rates can remain populated over extended time scales, enabling robust excitation trapping.

## B. Localization Control via Dominant Eigenmode under Transverse Modulation

To systematically explore how emitter geometry affects localization, we focus on the dominant eigenmode—defined as the mode with the largest contribution  $\max(w_i(t))$  at  $\gamma_0 t = 10^4$ . This mode is primarily responsible for the residual excitation observed at long times.

We examine how the decay rate of this dominant eigenmode,  $\gamma_{\text{dom}} = \text{Im}(\lambda_i)|_{\max(w_i(t))}$ , depends on the transverse modulation parameters  $\eta$  and  $\sigma$  that define the single- and double-Gaussian profiles [Eqs. (5) and (6)]. These geometries control the spatial variation of the emitter-waveguide coupling, which in turn influences the formation of subradiant modes.

For the single-Gaussian case at fixed  $\xi = 0.15\pi$ , increasing  $\eta$  while holding  $\sigma = 0.2$  leads to an exponential suppression of the decay rate, as shown in Fig. 3(a), indicating enhanced localization due to reduced collective coupling. When  $\eta = 0.05$  is held fixed and  $\sigma$  is varied, the decay rate reaches a minimum near  $\sigma = 0.1$ , as seen in Fig. 3(b). For larger  $\sigma$ , the smoother profile weakens localization as the geometry approaches a uniform linear array. The full parameter dependence is illustrated in Fig. 3(c), where a distinct region of minimized decay identifies an optimal regime for long-lived excitation trapping.

A similar analysis for the double-Gaussian configuration at  $\xi = 0.25\pi$  yields analogous trends. Increasing  $\eta$  at fixed  $\sigma = 0.075$  suppresses the decay rate monotonically [Fig. 3(d)]. When  $\eta = 0.05$  is fixed and  $\sigma$  is varied, the decay rate exhibits a local minimum around  $\sigma = 0.05$ , as shown in Fig. 3(e). Although an even smaller decay rate appears around  $\sigma = 0.35$ , this configuration no longer preserves the double-Gaussian structure; instead, the profile effectively becomes a single broad Gaussian, losing the intended geometric separation. The full parameter dependence is summarized in the colormap shown in Fig. 3(f), which maps the dominant decay

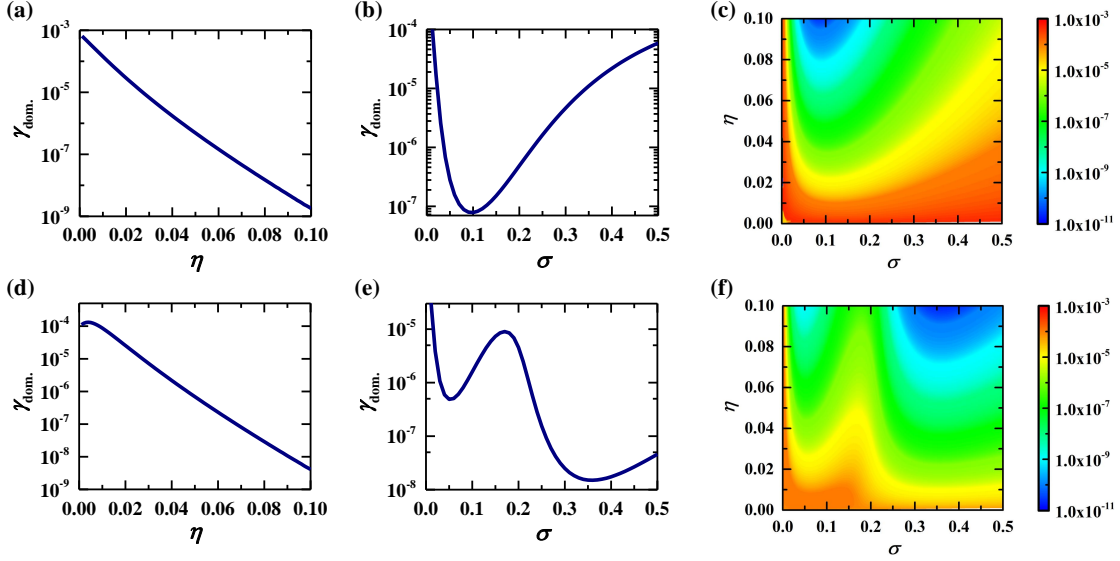


FIG. 3. (a), (b) Decay rate of the dominant eigenmode of the non-Hermitian Hamiltonian  $H_{\text{eff}}$  for emitters arranged in a single-Gaussian transverse profile [Eq. (5)], with  $\xi = 0.15\pi$ . In (a),  $\sigma = 0.2$  is fixed while  $\eta$  is varied, showing an exponential suppression of the decay rate as  $\eta$  increases. In (b),  $\eta = 0.05$  is fixed and the decay rate exhibits a minimum around  $\sigma = 0.1$ , suggesting an optimal configuration for minimizing radiative loss. (c) Colormap of the decay rate as a function of both  $\sigma$  and  $\eta$ . (d), (e) Decay rate of the dominant eigenmode for emitters arranged in a double-Gaussian transverse profile [Eq. (6)], with  $\xi = 0.25\pi$ . In (d),  $\sigma = 0.075$  is fixed and  $\eta$  is varied, leading to a monotonic reduction in decay rate with increasing  $\eta$ . In (e),  $\eta = 0.05$  is fixed and the decay rate shows a local minimum near  $\sigma = 0.05$ . A secondary minimum appears around  $\sigma = 0.35$ , configuration no longer retains the intended double-Gaussian structure. (f) Colormap of the decay rate across the  $(\sigma, \eta)$  parameter space, identifying regions that support strongly subradiant dominant modes.

rate across the  $(\eta, \sigma)$  space. Strong localization is achieved within a narrow region where the spatial configuration maintains well-separated peaks and sufficient transverse displacement ( $\sigma \sim 0.05$ ).

These results demonstrate that by tuning the transverse geometry of the emitter array, one can control both the lifetime and spatial structure of the dominant eigenmode. This provides a powerful route to engineering long-lived, spatially localized excitations in waveguide QED systems.

#### IV. EFFECT OF DISORDER ON DIFFERENT EMITTER ARRANGEMENTS

In this section, we study how the introduction of disorder affects the localization properties of emitter arrays that are originally structured to support geometry-induced localization. We compare three representative spatial configurations: a linear array, a single-Gaussian profile, and a double-Gaussian profile. The system parameters are chosen based on the findings from the previous section: for both the linear and single-Gaussian arrangements, we consider  $N = 101$  emitters with an inter-emitter spacing of  $\xi = 0.15\pi$ . This choice ensures that, in the absence of disorder, the single-Gaussian configuration supports localization dominated by a single long-lived eigenmode at long times. By restricting the dynamics to a single mode, we avoid complications arising from multi-mode interference, thereby facilitating a clearer analysis of

disorder effects. In contrast, for the double-Gaussian arrangement, the same inter-emitter spacing yields negligible long-time population; thus, we adopt  $N = 151$  emitters to enhance dipole-dipole interactions and maintain sufficient population trapping. These settings allow a consistent and meaningful comparison of disorder-induced modifications across different geometries.

##### A. Linear Arrangement

We begin by analyzing a linear array of two-level quantum emitters initialized in a symmetric Dicke state. In this configuration, the transverse displacement is set to zero for all emitters, such that  $y_\mu = 0$ . The time evolution of the remaining population  $P(t)$  under increasing disorder  $W_\mu$  is shown in Figs. 4(a). As the disorder strength increases, a larger fraction of the excitation remains in the system, indicating a progressive suppression of radiative decay.

The corresponding spatial distribution of the excitation at a long time  $\gamma_0 t = 10^4$  is shown in Fig. 4(b). For weak disorder, the spatial profile remains approximately Gaussian, while for stronger disorder, it becomes irregular but remains concentrated near the center of the chain. These results suggest that disorder leads to the formation of more localized and longer-lived subradiant modes.



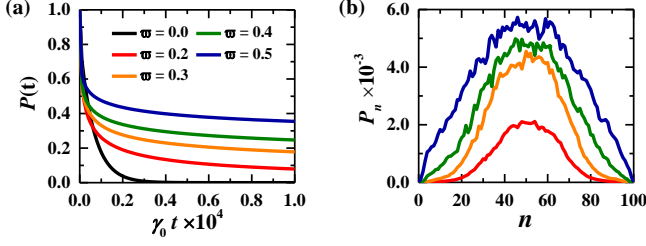


FIG. 4. (a) Time evolution of the total remaining population in a linearly arranged emitter array under increasing disorder. The system comprises  $N = 101$  uniformly spaced emitters with inter-emitter spacing  $\xi = 0.15\pi$  and zero transverse displacement. (b) Spatial population distributions at  $\gamma_0 t = 10^4$  for selected disorder strengths. Parameter values and color coding match those used in (a).

### B. Single-Gaussian Arrangement

We next consider a single-Gaussian emitter arrangement defined in Eq. (5), with  $\eta = 0.05$  and  $\sigma = 0.2$ . In this configuration, the emitters remain uniformly spaced along the propagation axis, while the transverse displacements create a smoothly varying emitter-waveguide coupling strength across the array. The time evolution of the remaining population  $P(t)$  under increasing disorder  $W_\mu$  is shown in Fig. 5(a). Even in the absence of disorder, significant population trapping occurs due to the site-dependent coupling strengths, which suppress collective emission and lead to the formation of a long-lived localized mode. As disorder is introduced, the trapped population initially decreases, indicating that geometry-induced localization is sensitive to perturbations. Upon further increasing the disorder strength, the population begins to recover and eventually surpasses the clean-case level, suggesting a crossover from geometry-induced to disorder-induced localization.

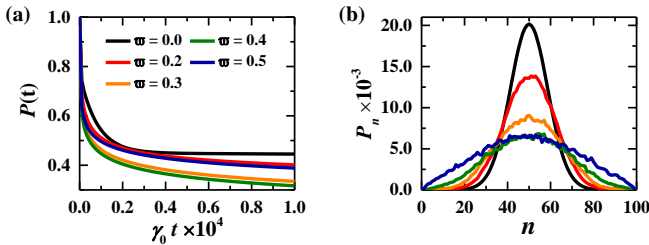


FIG. 5. (a) Time evolution of the total remaining population for emitters arranged in a single-Gaussian transverse profile, with parameters  $\eta = 0.05$ ,  $\sigma = 0.2$ ,  $N = 101$ , and  $\xi = 0.15\pi$ . Moderate disorder reduces the effect of geometry-induced localization, while stronger disorder restores trapping via disorder-induced localization. (b) Population distributions at  $\gamma_0 t = 10^4$  for selected disorder strengths. In the absence of disorder, spatial modulation of the coupling leads to geometry-induced localization near the center of the array. Parameter values and color coding match those used in (a).

The spatial excitation distributions at a long time of  $\gamma_0 t = 10^4$  provide additional insight into the effect of disorder.

At zero disorder, the population profile resembles a smooth Gaussian, reflecting the underlying symmetry of the emitter geometry. As disorder strength increases, the profile becomes increasingly irregular while remaining centered around the middle of the array, as shown in Figs. 5(b).

While a crossover from geometry-induced to disorder-induced localization is also present in the single-Gaussian configuration, this transition is not readily visible in the spatial distributions. Both mechanisms tend to produce centrally localized excitation profiles, making it difficult to infer the dominant localization mechanism based solely on the shape of the distribution. This limitation motivates the introduction of a more structured geometry—namely, the double-Gaussian profile—which enables a clearer visualization of the localization crossover.

### C. Double-Gaussian Arrangement

We finally examine the double-Gaussian emitter arrangement defined in Eq. (6), with  $\eta = 0.05$  and  $\sigma = 0.075$ . In this setup, the emitters are spatially configured to create two regions of weak coupling to the waveguide, producing distinct localization behavior. The evolution of the remaining population  $P(t)$  under varying disorder strength is depicted in Figs. 6(a). Upon the introduction of disorder, the trapped population initially diminishes, indicating that geometry-induced localization is sensitive to perturbations. As the disorder strength increases further, the population begins to recover and eventually exceeds the clean-case value, consistent with a crossover from geometry-driven to disorder-driven localization.

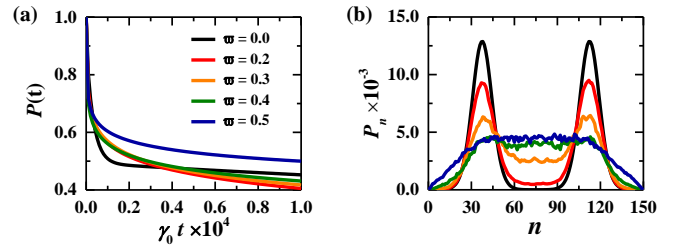


FIG. 6. (a) Time evolution of the total remaining population for emitters arranged in a double-Gaussian transverse profile, with parameters  $\eta = 0.05$ ,  $\sigma = 0.075$ ,  $N = 151$  and  $\xi = 0.15\pi$ . Results are shown under increasing axial disorder. (b) Spatial excitation distributions at  $\gamma_0 t = 10^4$  for selected disorder strengths. In the clean limit, excitation is localized in two distinct regions corresponding to weakly coupled emitter clusters. As disorder increases, the peaks become less well-defined and partially overlap, indicating a deformation of the original geometry-induced profile.

Further insights into the dynamics are revealed by examining the spatial excitation profile at a long evolution time of  $\gamma_0 t = 10^4$ . In the clean limit ( $\bar{\omega} \approx 0$ ), the distribution exhibits two clearly resolved Gaussian-like peaks, corresponding to the engineered regions of minimal coupling. As disorder

der increases, the initially well-separated peaks become less distinct and gradually merge into a single broad distribution centered in the array, as shown in Fig. 6(c). This transformation captures a transition between distinct localization mechanisms: at low disorder, excitation confinement is governed by geometry-induced subradiance, while at higher disorder, random scattering dominates and drives disorder-induced localization.

## V. SIZE EFFECTS

To investigate how system size influences population trapping in the presence of disorder, we examine the total excitation population remaining at a long time  $\gamma_0 t = 10^4$  as a function of the number of emitters  $N$ . Results for three emitter configurations—linear, single-Gaussian, and double-Gaussian—are shown in Fig. 7. All three configurations are based on a fixed inter-emitter spacing of  $\xi = 0.15\pi$ . The single-Gaussian profile is defined by transverse modulation parameters  $\eta = 0.05$  and  $\sigma = 0.2$ , while the double-Gaussian configuration uses  $\eta = 0.05$  and  $\sigma = 0.075$ .

In the linear configuration [Figures 7(a)], population trapping is unexpectedly strong for large  $N$  in the clean limit due to subradiant modes supported by the spatial symmetry of the system. These modes originate from destructive interference that inhibits collective decay. However, even weak disorder breaks this symmetry and rapidly suppresses the subradiant behavior. At higher disorder strengths, Anderson-like localization becomes the dominant mechanism, leading to a recovery in population trapping.

The single-Gaussian configuration [Figures 7(b)] exhibits more stable population retention across a wide range of system sizes, particularly at low to moderate disorder strengths. This robustness arises from geometry-induced spatial variation in emitter-waveguide coupling. In this profile, emitters near the center are transversely displaced furthest from the waveguide and therefore couple only weakly to the photonic reservoir. As the system size increases, emitters are added throughout the array, including both central and peripheral regions. However, the long-time dynamics remain dominated by excitation confined to the weakly coupled central region. Emitters located farther from the center experience stronger coupling and tend to decay more rapidly, contributing little to the population that persists at late times.

The double-Gaussian configuration [Figures 7(c)] exhibits population trapping that depends sensitively on system size and disorder strength. At low disorder strengths, the system effectively behaves as two spatially separated single-Gaussian segments, and therefore requires a larger number of emitters for significant population trapping. As disorder increases, the distinction between the two lobes becomes less significant, and the system begins to support long-lived modes with enhanced excitation confinement. This transition reflects a shift in the dominant localization mechanism, from geometry-induced subradiance to disorder-induced localization.

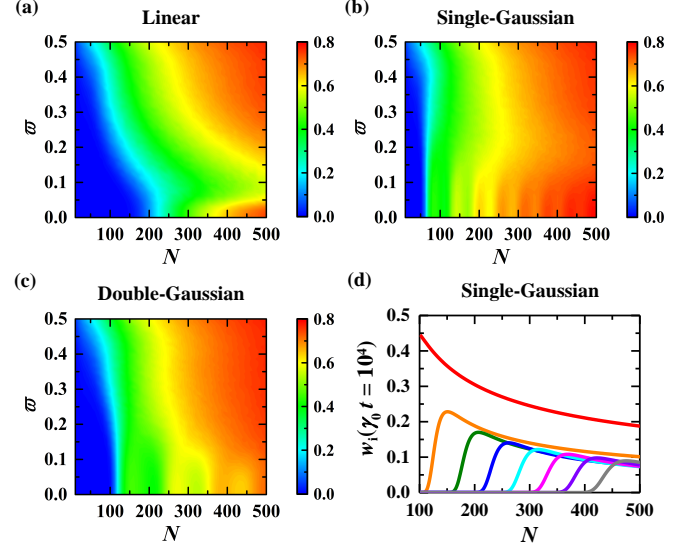


FIG. 7. Total population remaining at time  $\gamma_0 t = 10^4$  as a function of emitter number  $N$  and disorder strength  $W_\mu$  for three emitter configurations: (a) linear, (b) single-Gaussian, and (c) double-Gaussian. (d) Contribution at  $\gamma_0 t = 10^4$  as the emitter number  $N$  changes. The red line represents the contribution of the 1st mode, orange is for the 2nd mode, green for the 3rd mode, blue for the 4th mode, cyan for the 5th mode, magenta for the 6th mode, purple for the 7th mode, and gray for the 8th mode.

In both the single-Gaussian and double-Gaussian configurations, ripples in the remaining population are observed in the clean limit as the number of emitters  $N$  increases [Figures 7(b) and (c)]. This behavior can be attributed to two factors: first, the increasing number of subradiant modes as  $N$  grows, which leads to a redistribution of the population among these modes; second, some of these subradiant modes experience a decrease in their decay rates. These two factors combined cause the trapped population to exhibit ripples as the system size increases. For the single-Gaussian configuration, these ripples are most pronounced when  $N$  is in the range of 100 to 350, where the number of remaining long-lived modes at  $\gamma_0 t = 10^4$  increases from one to six [Figures 7(d)]. As more long-lived modes become available, the population becomes more evenly distributed among them, leading to a reduction in the amplitude of the ripples. This explains why ripples are no longer observed for  $N \gtrsim 350$ , where a sufficiently large number of modes results in a smooth population distribution. Additionally, as  $N$  increases, the number of subradiant modes contributing to the dynamics also increases, and the position of the ripple aligns with the peak value of the  $i$ th subradiant mode's contribution [Figures 7(b) and (d)], showing that the excitation trapping is directly related to the contribution of these modes. A similar trend is observed in the double-Gaussian configuration. However, as disorder increases, this effect diminishes. Since disorder lacks a specific geometric structure, the population distribution becomes more uniform on average, and the ripple effect vanishes as the system becomes dominated by disorder-induced localization.

## VI. DISCUSSION AND CONCLUSION

In this work, we have investigated excitation localization and population trapping in one-dimensional arrays of quantum emitters coupled to a waveguide, focusing the interplay between engineered emitter geometries and static disorder. Using time-domain simulations combined with biorthogonal eigenspectrum analysis of the non-Hermitian effective Hamiltonian [43], we identified two distinct mechanisms of localization in open quantum systems: geometry-induced subradiance and disorder-induced Anderson-like localization [39, 40, 42, 53].

Our results show that spatially modulated emitter arrangements—such as single- and double-Gaussian transverse profiles—can support long-lived collective modes with significantly reduced decay rates compared to uniform arrays. These subradiant modes arise from inhomogeneous coupling to the waveguide and are highly sensitive to the transverse emitter distribution. Through systematic parameter mapping, we identified geometric regimes that optimize population trapping and coherence retention.

In contrast, localization in uniform linear arrays requires sufficient disorder to break spatial symmetry and enable interference-based confinement. By varying disorder strength, we observed a crossover from geometry-induced to disorder-induced localization. This transition is subtle in single-Gaussian configurations, but becomes pronounced in double-Gaussian arrays, where the spatial excitation pattern evolves from a double-peaked profile to a broad, centrally localized distribution, indicating a transition from geometry-induced to disorder-induced confinement.

We further examined the impact of system size, showing that geometry-induced localization remains effective in large arrays. This suggests a practical advantage over disorder-based or symmetry-protected localization schemes, particularly in the context of scalability and experimental implementation.

These findings provide new insights into how spatial geometry and disorder can be used as complementary tools to control decoherence and dissipation in waveguide QED systems. The predicted localization behavior and enhanced excitation lifetimes are directly relevant to ongoing experiments with cold atoms coupled to nanophotonic structures [46, 47], superconducting qubits coupled via microwave waveguides [44, 45], and solid-state emitters embedded in photonic crystals [3].

Looking ahead, several promising directions remain, including extending the analysis to the multi-excitation regime and incorporating temporal disorder or nonlinear interactions. In addition, introducing chiral coupling—asymmetric emission into left- and right-propagating modes—would provide a promising route to explore nonreciprocal localization dynamics and direction-dependent subradiance. By bridging theoretical predictions with practical implementations, our findings pave the way for designing scalable, coherent quantum

networks and quantum memories with enhanced control over dissipation and decoherence.

## ACKNOWLEDGMENTS

We acknowledge support from the National Science and Technology Council (NSTC), Taiwan, under the Grant No. NSTC-112-2119-M-001-007, No. NSTC-112-2112-M-001-079-MY3, No. NSTC-113-2112-M-002-025, and No. NSTC-112-2112-M-002-001, and from Academia Sinica under Grant AS-CDA-113-M04. We are also grateful for support from TG 1.2 of NCTS at NTU.

\* [lcy511085@gmail.com](mailto:lcy511085@gmail.com)

† [alex968.tw@gmail.com](mailto:alex968.tw@gmail.com)

- [1] F. Le Kien, S. D. Gupta, K. P. Nayak, and K. Hakuta, *Physical Review A* **72**, 063815 (2005).
- [2] A. F. van Loo, A. Fedorov, K. Lalumière, B. C. Sanders, A. Blais, and A. Wallraff, *Science* **342**, 1494 (2013).
- [3] M. Arcari, I. Söllner, A. Javadi, S. Lindskov Hansen, S. Mahmoodian, J. Liu, H. Thyrrestrup, E. Lee, J. Song, S. Stobbe, and P. Lodahl, *Physical Review Letters* **113**, 093603 (2014).
- [4] J. S. Douglas, H. Habibian, C.-L. Hung, A. V. Gorshkov, H. J. Kimble, and D. E. Chang, *Nature Photonics* **9**, 326 (2015).
- [5] A. Goban, C.-L. Hung, J. Hood, S.-P. Yu, J. Muniz, O. Painter, and H. Kimble, *Physical Review Letters* **115**, 063601 (2015).
- [6] H. Pichler, T. Ramos, A. J. Daley, and P. Zoller, *Physical Review A* **91**, 042116 (2015).
- [7] E. Shahmoon, P. Grišins, H. P. Stimming, I. Mazets, and G. Kurizki, *Optica* **3**, 725 (2016).
- [8] J. Ruostekoski and J. Javanainen, *Physical Review Letters* **117**, 143602 (2016).
- [9] P. Lodahl, S. Mahmoodian, S. Stobbe, A. Rauschenbeutel, P. Schneeweiss, J. Volz, H. Pichler, and P. Zoller, *Nature* **541**, 473 (2017).
- [10] D. Chang, J. Douglas, A. González-Tudela, C.-L. Hung, and H. Kimble, *Reviews of Modern Physics* **90**, 031002 (2018).
- [11] S. Mahmoodian, G. Calajó, D. E. Chang, K. Hammerer, and A. S. Sørensen, *Physical Review X* **10**, 031011 (2020).
- [12] H. Le Jeannic, T. Ramos, S. F. Simonsen, T. Pognatolo, Z. Liu, R. Schott, A. D. Wieck, A. Ludwig, N. Rotenberg, J. J. García-Ripoll, and P. Lodahl, *Physical Review Letters* **126**, 023603 (2021).
- [13] O. A. Iversen and T. Pohl, *Physical Review Research* **4**, 023002 (2022).
- [14] A. S. Sheremet, M. I. Petrov, I. V. Iorsh, A. V. Poshakinskiy, and A. N. Poddubny, *Reviews of Modern Physics* **95**, 015002 (2023).
- [15] A. González-Tudela, A. Reiserer, J. J. García-Ripoll, and F. J. García-Vidal, *Nature Reviews Physics* **6**, 166 (2024).
- [16] F. Dinc, Å. Ercan, and A. M. Brańczyk, *Quantum* **3**, 213 (2019).
- [17] G. Fedorovich, D. Kornovan, A. Poddubny, and M. Petrov, *Physical Review A* **106**, 043723 (2022).
- [18] S. Cardenas-Lopez, S. J. Masson, Z. Zager, and A. Asenjo-Garcia, *Physical Review Letters* **131**, 033605 (2023).
- [19] C. Joshi, F. Yang, and M. Mirhosseini, *Physical Review X* **13**, 021039 (2023).
- [20] P. W. Anderson, *Physical Review* **109**, 1492 (1958).

- [21] M. O. Scully, [Physical Review Letters](#) **115**, 243602 (2015).
- [22] G. Facchinetti, S. D. Jenkins, and J. Ruostekoski, [Physical Review Letters](#) **117**, 243601 (2016).
- [23] H. H. Jen, M.-S. Chang, and Y.-C. Chen, [Physical Review A](#) **94**, 013803 (2016).
- [24] R. T. Sutherland and F. Robicheaux, [Physical Review A](#) **94**, 013847 (2016).
- [25] D. Plankensteiner, C. Sommer, H. Ritsch, and C. Genes, [Physical Review Letters](#) **119**, 093601 (2017).
- [26] S. D. Jenkins, J. Ruostekoski, N. Papisimakis, S. Savo, and N. I. Zheludev, [Physical Review Letters](#) **119**, 053901 (2017).
- [27] H. H. Jen, [Physical Review A](#) **96**, 023814 (2017).
- [28] D. Bhatti, R. Schneider, S. Oppel, and J. von Zanthier, [Physical Review Letters](#) **120**, 113603 (2018).
- [29] M. Moreno-Cardoner, D. Plankensteiner, L. Ostermann, D. E. Chang, and H. Ritsch, [Physical Review A](#) **100**, 023806 (2019).
- [30] A. Albrecht, L. Henriët, A. Asenjo-Garcia, P. B. Dieterle, O. Painter, and D. E. Chang, [New Journal of Physics](#) **21**, 025003 (2019).
- [31] Y.-X. Zhang and K. MÄžlmer, [Physical Review Letters](#) **122**, 203605 (2019).
- [32] G. Ferioli, A. Glicenstein, L. Henriët, I. Ferrier-Barbut, and A. Browaeys, [Physical Review X](#) **11**, 021031 (2021).
- [33] M. Moreno-Cardoner, R. Holzinger, and H. Ritsch, [Optics Express](#) **30**, 10779 (2022).
- [34] T. Hsu, K.-T. Lin, and G.-D. Lin, [New Journal of Physics](#) **26**, 053026 (2024).
- [35] H. H. Jen, [Quantum Science and Technology](#) **10**, 023001 (2025).
- [36] T. Schwartz, G. Bartal, S. Fishman, and M. Segev, [Nature](#) **446**, 52 (2007).
- [37] Y. Lahini, A. Avidan, F. Pozzi, M. Sorel, R. Morandotti, D. N. Christodoulides, and Y. Silberberg, [Physical Review Letters](#) **100**, 013906 (2008).
- [38] T. F. See, V. M. Bastidas, J. Tangpanitanon, and D. G. Angelakis, [Physical Review A](#) **99**, 033835 (2019).
- [39] H. H. Jen, M.-S. Chang, G.-D. Lin, and Y.-C. Chen, [Physical Review A](#) **101**, 023830 (2020).
- [40] H. H. Jen, [Physical Review A](#) **105**, 023717 (2022).
- [41] D. Sels, [Physical Review B](#) **106**, 1020202 (2022).
- [42] C.-C. Wu, K.-T. Lin, I. G. N. Y. Handayana, C.-H. Chien, S. Goswami, G.-D. Lin, Y.-C. Chen, and H. H. Jen, [Physical Review Research](#) **6**, 013159 (2024).
- [43] G. G. Giusteri, F. Mattiotti, and G. L. Celardo, [Physical Review B](#) **91**, 094301 (2015).
- [44] P. Roushan, C. Neill, J. Tangpanitanon, V. M. Bastidas, A. Megrant, R. Barends, Y. Chen, Z. Chen, B. Chiaro, A. Dunsworth, A. Fowler, B. Foxen, M. Giustina, E. Jeffrey, J. Kelly, E. Lucero, J. Mutus, M. Neeley, C. Quintana, D. Sank, A. Vainsencher, J. Wenner, T. White, H. Neven, D. G. Angelakis, and J. Martinis, [Science](#) **358**, 1175 (2017).
- [45] K. Xu, J.-J. Chen, Y. Zeng, Y.-R. Zhang, C. Song, W. Liu, Q. Guo, P. Zhang, D. Xu, H. Deng, K. Huang, H. Wang, X. Zhu, D. Zheng, and H. Fan, [Physical Review Letters](#) **120**, 050507 (2018).
- [46] M. E. Kim, T.-H. Chang, B. M. Fields, C.-A. Chen, and C.-L. Hung, [Nature Communications](#) **10**, 10.1038/s41467-019-09635-7 (2019).
- [47] X. Luan, J. Béguin, A. P. Burgers, Z. Qin, S. Yu, and H. J. Kimble, [Advanced Quantum Technologies](#) **3**, 10.1002/qute.202000008 (2020).
- [48] A. González-Tudela and D. Porras, [Physical Review Letters](#) **110**, 080502 (2013).
- [49] H. H. Jen, [Physical Review A](#) **102**, 043525 (2020).
- [50] R. H. Lehmborg, [Physical Review A](#) **2**, 883 (1970).
- [51] R. H. Dicke, [Physical Review](#) **93**, 99 (1954).
- [52] K. Stannigel, P. Rabl, and P. Zoller, [New Journal of Physics](#) **14**, 063014 (2012).
- [53] H. H. Jen and J.-S. You, [Journal of Physics B: Atomic, Molecular and Optical Physics](#) **54**, 105002 (2021).